(Received 15 June 2026, Accepted 15 July 2026, Scheduled 14 August 2026)

A Flexible Passive Metasurface Reflector for Absorption, Linear-to-Linear, and Linear-to-Circular Polarization Conversion

Ke Wang[1,2,*], Hao Fei Zhang[3], Long Sheng Li[1], Chun Lei Xu[1],
Yi Chao Zhou[1,2], and Shi Jie Xie[1,2]

[1]School of Information Engineering, Jiangsu College of Engineering and Technology, Nantong, China
[2]Nantong Key Laboratory of Artificial Intelligence New Quality Technology
Jiangsu College of Engineering and Technology, Nantong, China
[3]Purple Mountain Laboratories, Nanjing, China

ABSTRACT: A flexible multifunctional passive metasurface reflector is proposed, which integrates broadband absorption, linear-to-linear polarization conversion, and dual-band linear-to-circular polarization conversion on a single passive platform. The proposed unit cell consists of a circular split-ring resonator and X-shaped metallic patches loaded with lumped resistors. The metallic patterns were fabricated on a flexible polyimide (PI) substrate, followed by a polymethacrylimide (PMI) spacer layer and a metallic ground plane. Without employing any active components, the metasurface achieves an absorptivity higher than 90% over the 4.45–8.46 GHz band. In the 12.1–15.2 GHz frequency range, the polarization conversion ratio exceeds 90%, enabling efficient linear-to-linear polarization conversion. Furthermore, within the frequency bands of 16.5–17.3 GHz and 17.7–18.2 GHz, the proposed metasurface converts incident linearly polarized waves into right-handed circularly polarized (RHCP) and left-handed circularly polarized (LHCP) waves, respectively, while the output handedness can be interchanged by rotating the incident polarization by 90°. Conformal measurements demonstrate that the proposed metasurface maintains stable absorption performance under moderate bending, with only slight degradation in polarization conversion performance and a small frequency shift in the circular polarization conversion bands. Experimental measurements show good agreement with simulated results, verifying the effectiveness of the proposed design. Owing to its simple configuration, low cost, multifunctional integration, and conformal capability, the proposed metasurface provides a promising solution for multifunctional electromagnetic manipulation in conformal integrated electromagnetic systems.

1. INTRODUCTION

Metasurfaces, which are two-dimensional planar devices composed of subwavelength artificial structural elements, have demonstrated remarkable capabilities in electromagnetic wave manipulation [1–3]. By carefully engineering the arrangement of unit cells, metasurfaces can flexibly control the phase, amplitude, and polarization of electromagnetic waves. Due to their multifunctional characteristics, metasurfaces have shown broad application prospects in polarization conversion, electromagnetic absorption, holographic imaging, antenna gain enhancement, beam shaping, and planar lens design [4–9]. Among these applications, metasurface-based polarization converters and absorbers have attracted considerable attention due to their potential in radar cross-section (RCS) reduction and polarization control. To manipulate the polarization state of electromagnetic waves, various metasurface-based polarization converters have been developed, including linear-to-cross polarization converters and linear-to-circular polarization converters [10, 11]. Meanwhile, broadband absorbers based on impedance matching and resonant loss mechanisms have also been extensively investigated [12, 13]. However, most reported metasurface designs are limited to a single functionality and can only perform one specific operation, which restricts their potential applications in highly integrated electromagnetic systems.

To address this issue, many studies have employed multi-resonance structural patterns to realize multifunctional devices [14–16]. This approach offers advantages such as simple configuration, ease of fabrication, and compactness. However, existing works are generally limited either by operational bandwidth or by the number of achievable functionalities. In recent years, the research focus has gradually shifted from realizing multiple microwave functions to multifunctional integrated and multispectral-compatible metasurfaces. Beyond conventional microwave electromagnetic manipulation, state-of-the-art metasurfaces have demonstrated simultaneous integration of microwave absorption or polarization control with visible-light transparency or dynamic coloration, infrared thermal radiation regulation, and thermal management, enabling multifunctional operation across microwave, visible, and infrared spectral regimes within a single planar architecture [17–21]. These multispectral-compatible metasurfaces significantly broaden the application scope of metasurfaces in electromagnetic stealth, intelligent camouflage, and integrated

* Corresponding author: Ke Wang (wangke_nt@hotmail.com).

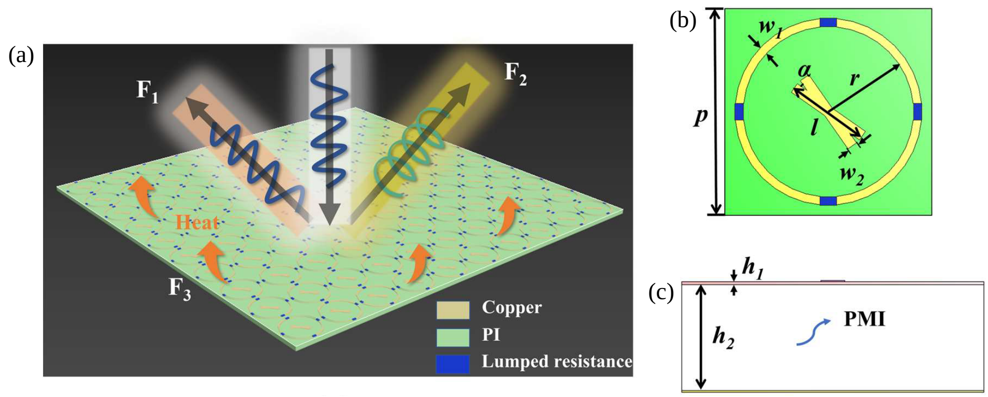

FIGURE 1. (a) Functional schematic of a reflective metasurface: F_1 denotes linear polarization conversion, F_2 denotes circular polarization conversion, and F_3 denotes electromagnetic wave absorption. (b) Top view of the unit cell. (c) Side view of the unit cell ($P = 18\,\text{mm}$, $w_1 = 0.8\,\text{mm}$, $w_2 = 1\,\text{mm}$, $r = 8\,\text{mm}$, $l = 7\,\text{mm}$, $a = 15^\circ$, $h_1 = 0.1\,\text{mm}$, $h_2 = 6\,\text{mm}$.)

electromagnetic-thermal systems. Meanwhile, another important research direction is the development of dynamically reconfigurable and programmable metasurfaces [22–24]. By incorporating active components into unit cells, metasurfaces can switch between two or more electromagnetic functionalities, thereby significantly expanding their application scenarios. Although switchable metasurfaces provide flexible functional reconfigurability, introducing active elements inevitably requires additional biasing networks, which increases both device volume and system complexity.

This paper proposes a tri-functional metasurface capable of simultaneously achieving multiple electromagnetic functionalities over a broad frequency range via incorporating lumped elements. Specifically, the proposed metasurface operates as an absorber within 4.45–8.46 GHz, functions as a cross-polarization converter in the 12.1–15.2 GHz band, and realizes linear-to-circular polarization conversion within two adjacent frequency bands of 16.5–17.3 GHz and 17.7–18.2 GHz, generating left-handed circular polarization (LHCP) and right-handed circular polarization (RHCP), respectively. Moreover, the output handedness can be interchanged when the incident polarization is rotated orthogonally. The proposed metasurface has low cost and a simple structure, and both its absorption and polarization-conversion characteristics exhibit broadband performance. Unlike most existing multifunctional metasurface designs, the proposed scheme achieves multifunctional integration without relying on any tunable components. In addition, the introduction of a flexible substrate significantly extends its applicability in practical engineering scenarios. Simulated and experimental results were in good agreement, and conformal measurements further verified the reliable performance of the proposed flexible metasurface under curved-surface conditions.

2. STRUCTURE AND FUNCTIONALITY

2.1. Structure of the Proposed Element

The unit structure of the proposed multifunctional metasurface is shown in Fig. 1(a). It adopts a conventional sandwich-like layered configuration consisting of a patterned layer, dielectric substrate layer, and metallic ground plane from top to bottom. The patterned layer is composed of a circular split-ring resonator and an X-shaped copper pattern, and the blue regions represent lumped resistors. The substrate layer was made of a flexible polyimide (PI) material with a relative permittivity of $\varepsilon_r = 3.5$ and a loss tangent of $\tan\delta = 0.008$. The substrate was bonded to the metallic ground plane through a polymethacrylimide (PMI) layer to ensure structural stability. The metallic ground plane was realized using a 0.018 mm thick copper sheet to eliminate electromagnetic transmission through the metasurface. The optimized geometrical parameters are summarized in Fig. 1.

The proposed structure evolves through several design stages, as shown in Fig. 2. Full-wave simulations of the metasurface unit cell were performed using the commercial electromagnetic simulation software Computer Simulation Technology (CST) Microwave Studio. Unit-cell boundary conditions were applied along the x- and y-directions, whereas Floquet ports were assigned along the z-direction for excitation. An x-polarized electromagnetic wave was normally incident on the top surface of the structure, and the co-polarized reflection coefficient r_{xx} and cross-polarized reflection coefficient r_{yx} for each design stage are shown in Fig. 2(b).

For Step 1 in Fig. 2(b), the frequency response clearly shows that both r_{xx} and r_{yx} are lower than -10 dB at 14.2 GHz and 16.1 GHz, indicating strong absorption characteristics at these two resonant frequencies. By introducing lumped resistors, as shown in Step 2, the absorption performance is significantly enhanced. In particular, both r_{xx} and r_{yx} remain below -10 dB within the 4.4–8.5 GHz frequency range, demonstrating broadband absorption and indicating a substantial expansion of absorption bandwidth.

To further endow the metasurface with multifunctional characteristics, an X-shaped structure was embedded inside the circular ring, resulting in the configuration shown in Step 3, which corresponds to the final proposed design in this work. The simulated results of Step 3 reveal distinct electromagnetic responses over different frequency bands. In the low-frequency range (4.4–8.5 GHz), both r_{xx} and r_{yx} remain below -10 dB,

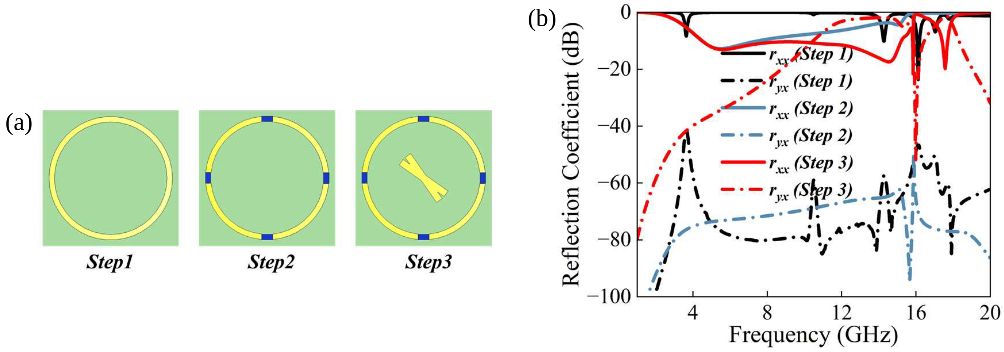

FIGURE 2. (a) Evolution of the proposed unit cell design. (b) Comparison of the co-polarized (r_{xx}) and cross-polarized (r_{yx}) reflection coefficients for the three design steps.

preserving the broadband absorption property. In the mid-frequency band (12–15.1 GHz), r_{yx} exceeds -3 dB while r_{xx} remains below -10 dB, indicating efficient cross-polarization conversion. In the high-frequency region, specifically within 16.5–17.3 GHz and 17.7–18.2 GHz, r_{xx} and r_{yx} approach similar magnitudes, implying the realization of linear-to-circular polarization conversion. These results demonstrate that the Step 3 design can function as both a low-frequency absorber and a high-frequency polarization converter, thereby validating the multifunctional electromagnetic response of the proposed metasurface.

2.2. Electromagnetic Responses of Element

The simulated and measured r_{xx} and r_{yx} responses of the proposed metasurface are shown in Fig. 3. In the frequency range of 4.4–8.5 GHz, both r_{xx} and r_{yx} remain below -10 dB, indicating good absorption performance. In the band from 11.6 to 15.2 GHz, r_{xx} is lower than -10 dB while r_{yx} exceeds -3 dB, indicating that the metasurface functions as a polarization converter. Moreover, within the frequency ranges of 16.5–17.3 GHz and 17.7–18.2 GHz, r_{xx} and r_{yx} exhibit nearly equal amplitudes with a phase difference of $\Delta\varphi \approx 90°$, confirming the realization of linear-to-circular polarization (LP-to-CP) conversion.

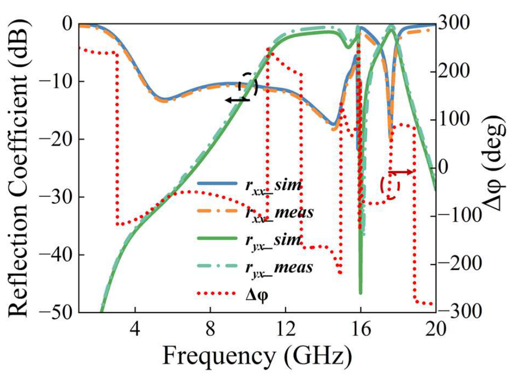

FIGURE 3. Frequency responses of r_{xx}, r_{yx}, and the corresponding phase difference $\Delta\varphi$.

2.3. Absorption Performance

The absorptivity A of the proposed metasurface can be calculated as [25]

$$A(\omega) = 1 - R(\omega) - T(\omega), \quad (1)$$

$$R(\omega) = \left|r_{xx}^2\right| + \left|r_{yx}^2\right|, \quad (2)$$

where ω denotes the angular frequency, and $R(\omega)$ and $T(\omega)$ represent the reflectivity and transmissivity, respectively. Due to the metallic ground plane, the transmissivity $T(\omega)$ is approximately zero. Fig. 4 shows the absorption performance of the proposed metasurface. It can be observed that the absorptivity exceeds 90% in the frequency range 4.45–8.46 GHz, with a maximum absorptivity 95% at 5.58 GHz.

2.4. Cross-Polarization Conversion

The proposed metasurface can also achieve broadband polarization conversion. For an x-polarized incident wave, the polarization conversion ratio (PCR) is defined as [26]

$$\text{PCR} = \left|r_{yx}^2\right| / \left(\left|r_{xx}^2\right| + \left|r_{yx}^2\right|\right). \quad (3)$$

Figure 5 shows the polarization conversion performance of the proposed metasurface. It can be observed that, within the frequency range of 11.6–15.2 GHz, the co-polarized reflection coefficient r_{xx} remains below -10 dB, while the cross-polarized reflection coefficient r_{yx} exceeds -3 dB. Correspondingly, the 3 dB relative bandwidth of r_{yx} reaches 3.6 GHz. In particular, the PCR exceeds 90% over the frequency range of 12.1–15.2 GHz, indicating that most of the incident x-polarized waves are efficiently converted into y-polarized reflected waves within this band.

2.5. Circular Polarization Conversion

In addition to the linear polarization conversion, the proposed metasurface can also achieve linear polarization to circular polarization (LP-to-CP) conversion. The axial ratio (AR), which is used to evaluate the purity of circular polarization, is defined as [27]

$$\text{AR} = \left(\frac{\left|r_{xy}\right|^2 + \left|r_{yy}\right|^2 + \sqrt{a}}{\left|r_{xy}\right|^2 + \left|r_{yy}\right|^2 - \sqrt{a}}\right)^{1/2}, \quad (4)$$

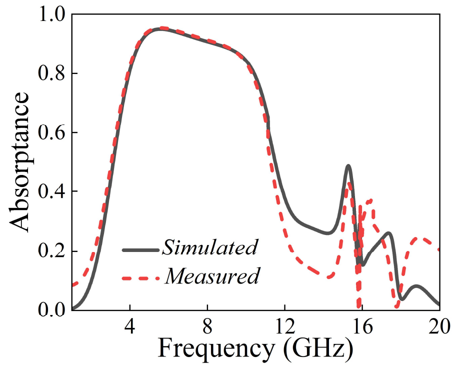

FIGURE 4. Simulated and measured absorption performance of the proposed metasurface.

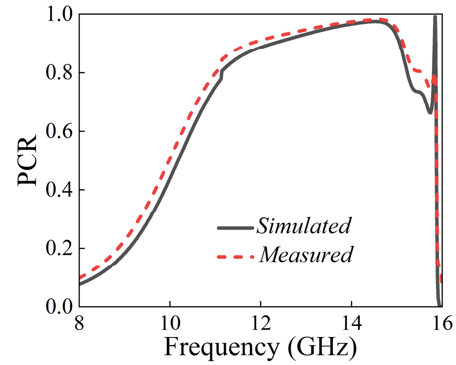

FIGURE 5. Simulated and measured PCR of the proposed metasurface.

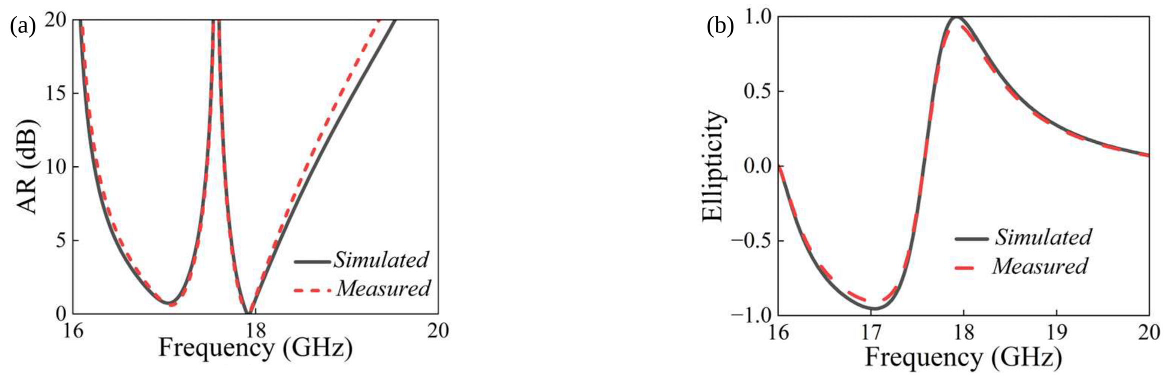

FIGURE 6. Simulated and measured results of the circular polarization conversion performance: (a) AR and (b) ellipticity.

where

$$a = |r_{xy}|^4 + |r_{yy}|^4 + 2\,|r_{xy}|^2\,|r_{yy}|^2 \cos(2\Delta\varphi). \tag{5}$$

Figure 6(a) illustrates the AR performance of the proposed metasurface. It can be observed that the frequency bands with AR less than 3 dB are 16.5–17.3 GHz and 17.7–18.2 GHz, corresponding to bandwidths of 0.8 GHz and 0.5 GHz, respectively. At 17.9 GHz, an AR value close to 0 dB and a phase difference of $\Delta\varphi \approx 90^\circ$ are obtained, indicating the perfect LP-to-CP conversion. Furthermore, the LP-to-CP conversion performance was further analyzed using the normalized ellipticity [16], which was calculated as follows:

$$e = \frac{2\,|r_{yx}|\,|r_{xx}|\sin\Delta\varphi}{|r_{yx}^2| + |r_{yx}^2|}. \tag{6}$$

As shown in Fig. 6(b), the ellipticity is close to -1 within the frequency range of 16.5–17.3 GHz, indicating that the reflected wave is RHCP in this band. Similarly, within the frequency range of 17.7–18.2 GHz, the ellipticity approaches $+1$, confirming that the reflected wave exhibits LHCP. These results verify that the proposed metasurface can realize orthogonal circular-polarization conversion at two distinct frequency bands.

2.6. Incident Angle Sensitivity Analysis

Figure 7 shows the performance of the proposed metasurface with different incident angles θ. For $\theta < 20^\circ$, the PCR bandwidth remains nearly unchanged, whereas it begins to decrease when $\theta > 20^\circ$, as shown in Fig. 7(a). From Fig. 7(b), it can be observed that the absorption bandwidth remains approximately constant. Notably, at larger incident angles, an increase in the absorption bandwidth is observed due to the merging of absorption peaks, as illustrated in Fig. 7(b), which may be attributed to the excitation of non-specular modes. Fig. 7(c) presents the AR variation under LP-to-CP conversion. As shown in Fig. 7(c), the AR remains nearly unchanged for small incident angles θ.

3. PRINCIPLE ANALYSIS

To further elucidate the operating mechanism of the proposed metasurface, an equivalent circuit model was established in Advanced Design System (ADS), as shown in Fig. 8(a). The metallic resonators are modeled using lumped inductive and capacitive elements. Specifically, coupling capacitance between adjacent unit cells is represented by C_0, while the dielectric loss is characterized by R_0. The equivalent inductances of the split-ring resonator and the X-shaped metallic patch are denoted by L_1 and L_2, respectively. Their mutual coupling is modeled by capacitors C_1 and C_2, and the lumped resistor is represented by R_1. In addition, the parasitic coupling between the metallic

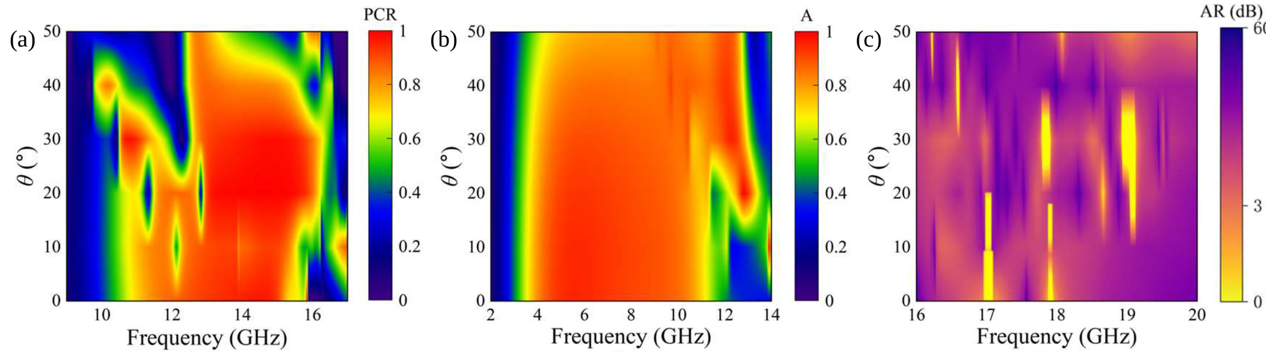

FIGURE 7. (a) PCR, (b) absorptance, and (c) AR under oblique incidence.

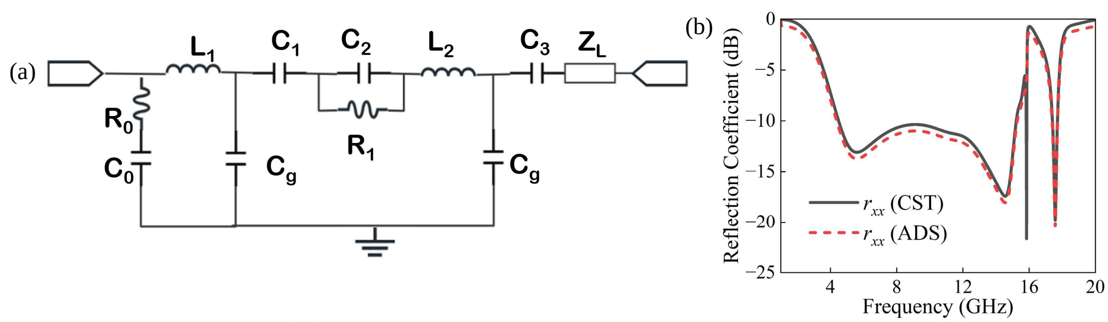

FIGURE 8. (a) Equivalent circuit of the unit cell. $C_0 = 0.03\,\text{pF}$, $L_1 = 3.56\,\text{nH}$, $R_0 = 0.38\,\Omega$, $C_1 = 0.05\,\text{pF}$, $C_2 = 0.063\,\text{pF}$, $L_2 = 2.1\,\text{nH}$, $C_g = 0.023\,\text{pF}$, $C_3 = 0.024\,\text{pF}$ and (b) comparison between the equivalent-circuit results and CST full-wave simulation.

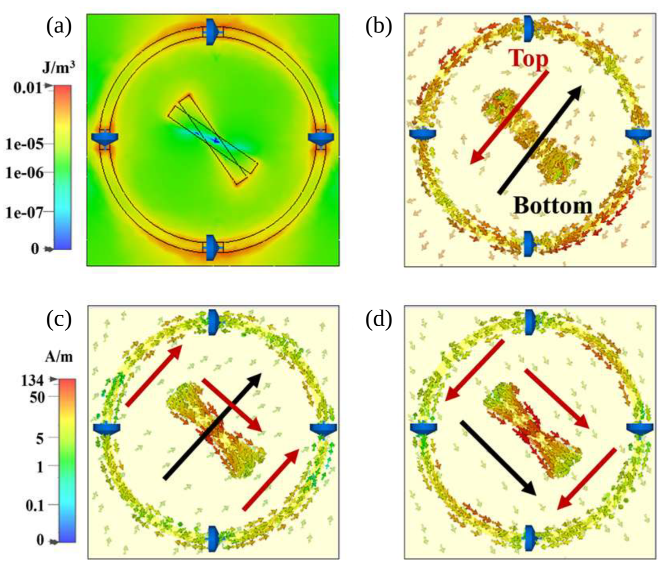

FIGURE 9. Power loss density and surface current distributions of the proposed metasurface at the representative resonant frequencies: (a) 5.58 GHz, (b) 15.1 GHz, (c) 17.1 GHz, and (d) 17.9 GHz.

pattern and the ground plane is modeled by the shunt capacitance C_g, and the input impedance of the grounded dielectric substrate is represented by the load impedance Z_L. By optimizing the equivalent circuit parameters, the reflection coefficient calculated from the circuit model agrees well with CST full-wave simulation results, as shown in Fig. 8(b), validating the effectiveness of the proposed equivalent circuit model and demonstrating its capability to accurately characterize the electromagnetic response of the proposed metasurface.

The power loss density and surface current distributions at representative resonant frequencies of 5.58, 15.1, 17.1, and 17.9 GHz are presented in Fig. 9. As shown in Fig. 9(a), the absorption mechanism originates from the strong power loss concentrated around the split-ring resonator and the central metallic pattern, where the incident electromagnetic energy is dissipated by dielectric loss and lumped resistors under good impedance matching. For linear polarization conversion, antiparallel surface currents induced on the top metallic layer and ground plane indicate the excitation of magnetic resonance, which suppresses co-polarized reflection while enhancing cross-polarized reflection. For LP-to-CP conversion, the induced surface currents flow along two orthogonal diagonal directions, establishing two reflected orthogonal field components with nearly equal amplitudes and a phase difference of $\pm 90°$. Consequently, the incident linearly polarized wave is converted into RHCP and LHCP reflected waves, respectively.

4. PERFORMANCE VALIDATION

For experimental verification, a metasurface prototype, as shown in Fig. 10(a), was fabricated using flexible printed circuit (FPC) technology. The fabricated sample consisted of 10×10 unit cells with an overall size of $180 \times 180\,\text{mm}^2$. The lumped resistors were implemented using SMD 0805 packages and soldered across the gaps between metallic patches. The polyimide film was fixed to the metallic ground plane using PMI foam to ensure structural stability. The reflection

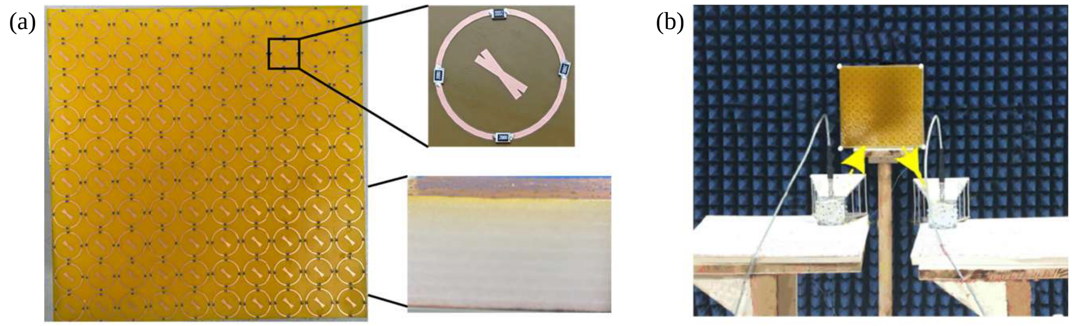

FIGURE 10. (a) Fabricated metasurface sample and (b) Measurement setup.

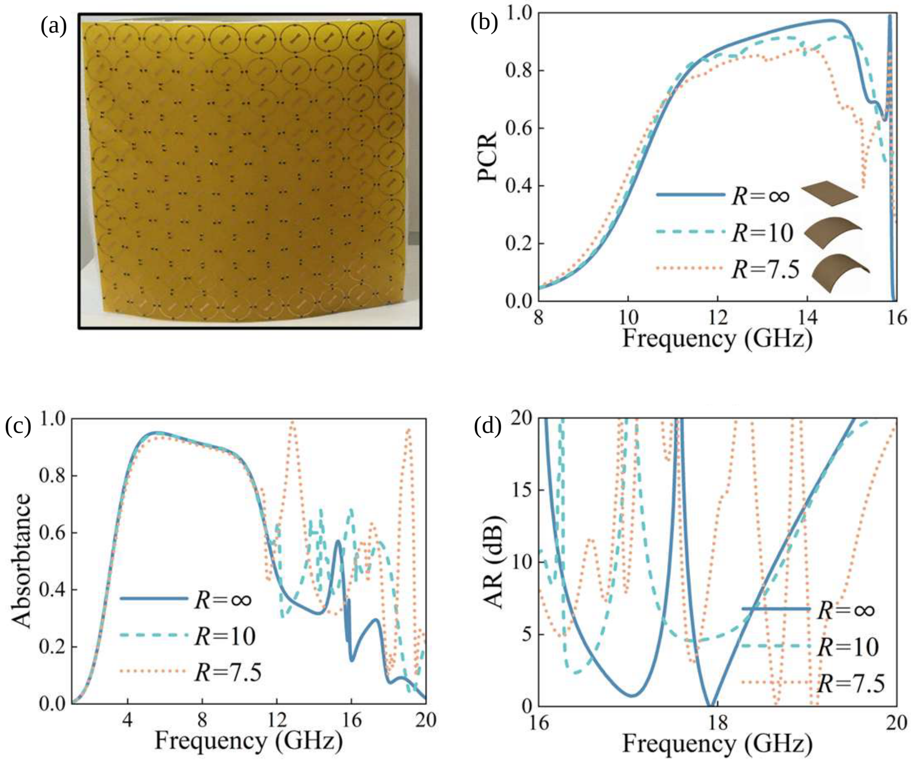

FIGURE 11. Conformal performance of the proposed metasurface under different bending conditions: (a) photograph of the conformal metasurface prototype, (b) PCR, (c) A, and (d) AR for bending radii of $R = \infty$ (flat), $R = 10$ cm, and $R = 7.5$ cm.

characteristics r_{xx} and r_{yx} of the fabricated metasurface were measured in a microwave anechoic chamber, as shown in Fig. 10(b). The measurement system consisted of a pair of horn antennas and a two-port vector network analyzer (Keysight N5230C). During the measurement of r_{xx}, the two horn antennas were arranged with the same polarization orientation. In contrast, for the measuring r_{yx}, the antennas were configured with orthogonal polarizations to obtain cross-polarized reflection response.

The measured results shown in Figs. 3–6 agree well with corresponding simulated results, demonstrating the effectiveness of the proposed metasurface. Minor discrepancies can be observed in several frequency regions and are mainly attributed to fabrication tolerances, soldering errors of SMD resistors, and measurement uncertainties. Nevertheless, the overall agreement between the simulated and measured results verifies the feasibility of the proposed design and the stability of its electromagnetic performance.

To evaluate the conformal performance of the proposed metasurface, conformal measurements were carried out under different bending conditions. As shown in Fig. 11(a), the fabricated sample was conformally attached to a cylindrical surface with a radius of $R = 10$ cm as a representative example. The corresponding PCR, A, and AR under different bending radii are presented in Figs. 11(b)–(d), respectively. Compared with the planar state, the PCR exhibits a slight degradation as the bending radius decreases, while the absorptivity remains nearly unchanged over the operating band, indicating that the absorption performance is well preserved under conformal deformation. In contrast, the circular polarization conversion performance exhibits a frequency shift, as evidenced by shifting AR operating band under bending conditions. These results indi-

TABLE 1. Comparison with previous works.

Ref.	Unit Size (λ_0)	Thickness (λ_0)	10 dB RCP (GHz)	3 dB AR (GHz)	A (GHz)	Flexible
[27]	0.16	0.14	-	5.8–20.4 (111.4%)	-	No
[11]	0.32	0.12	5.50–12.4 (77.1%)	13.50–19.75 (37.6%) for RHCP	-	No
[15]	0.29	0.08	10.3–15.26 (38.8%)	8.97–9.75 (8.33%), 17.51–23.93 (30.9%)	-	No
[25]	0.26	0.10	7.90–14.80 (60.7%)	-	3.78–6.34 (50.6%)	Yes
This work	0.26	0.09	12.1–15.2 (22.7%)	16.5–17.3 (4.7%) for RHCP 17.7–18.2 (2.8%) for LHCP	4.45–8.46 (62.1%)	Yes

λ_0: The wavelength corresponding to the lowest center frequency; RCP: Reflective cross polarization.

cate that the proposed metasurface can maintain its multifunctional electromagnetic characteristics under moderate bending, demonstrating good conformal capability for practical curved-surface applications.

Table 1 compares the performance of the proposed multifunctional metasurface with that of previously reported metasurfaces. The proposed design exhibits a compact unit size and a low profile, while maintaining conformal capability owing to its flexible substrate. Compared with previous multifunctional metasurfaces, it simultaneously integrates broadband absorption, linear-to-linear polarization conversion, and dual-band linear-to-circular polarization conversion within a single passive structure. Although its circular-polarization bandwidth is narrower than that of some reported designs, it offers a favorable balance among multifunctional integration, structural compactness, and flexibility.

5. CONCLUSION

In this paper, a multifunctional metasurface reflector was proposed and experimentally verified. By integrating a circular split-ring resonator, X-shaped patch, and lumped resistors into a single passive structure, three distinct electromagnetic functionalities, including broadband absorption, cross-polarization conversion, and circular polarization conversion, were realized without employing any active components or biasing networks. The proposed metasurface features a compact configuration and low fabrication costs. In addition, the use of a flexible polyimide substrate endows the structure with good conformal capability. Good agreement between the simulated and measured results validates the effectiveness of the proposed design. Furthermore, the conformal measurements under bending conditions demonstrate the reliability of the metasurface on curved surfaces, indicating its potential for electromagnetic manipulation applications involving complex-shaped platforms.

ACKNOWLEDGEMENT

This study was supported by the Jiangsu Province 333 High-level Talent Cultivation Project, Qinglan Project of Jiangsu Higher Education Institutions, Jiangsu Province Young Teachers Enterprise Practice Program (2025QYSJ104), Jiangsu Provincial High-Level Professional Group Program, and Natural Science Foundation of Jiangsu College of Engineering and Technology (JSGYZRJJYB-07).

REFERENCES

[1] Aieta, F., M. A. Kats, P. Genevet, and F. Capasso, "Multiwavelength achromatic metasurfaces by dispersive phase compensation," *Science*, Vol. 347, No. 6228, 1342–1345, 2015.

[2] Arbabi, A., E. Arbabi, Y. Horie, S. M. Kamali, and A. Faraon, "Planar metasurface retroreflector," *Nature Photonics*, Vol. 11, No. 7, 415–420, 2017.

[3] Chen, S., Z. Li, W. Liu, H. Cheng, and J. Tian, "From single-dimensional to multidimensional manipulation of optical waves with metasurfaces," *Advanced Materials*, Vol. 31, No. 16, 1802458, 2019.

[4] Huang, X., H. Yang, D. Zhang, and Y. Luo, "Ultrathin dual-band metasurface polarization converter," *IEEE Transactions on Antennas and Propagation*, Vol. 67, No. 7, 4636–4641, 2019.

[5] Luo, Z., X. Ren, L. Zhou, Y. Chen, Q. Cheng, H. F. Ma, and T. J. Cui, "A high-performance nonlinear metasurface for spatial-wave absorption," *Advanced Functional Materials*, Vol. 32, No. 16, 2109544, 2022.

[6] Yin, Y., Q. Jiang, H. Wang, and L. Huang, "Color holographic display based on complex-amplitude metasurface," *Laser & Photonics Reviews*, Vol. 19, No. 1, 2400884, 2025.

[7] Wang, K., W. Shao, X. Ding, B.-Z. Wang, and B. Jiang, "Design of high-gain metasurface antenna based on characteristic mode analysis," *IEEE Antennas and Wireless Propagation Letters*, Vol. 21, No. 4, 661–665, 2022.

[8] Zhang, J., W. Li, Y. Kang, T. Zou, X. Han, Y. Ying, J. Yu, J. Zheng, L. Qiao, J. Li, F. Qin, and S. Che, "Design of absorption-scattering integrated multi-layer metasurfaces for large-angle anomalous reflection," *Progress In Electromagnetics Research*, Vol. 183, 21–32, 2025.

[9] Jiang, X., C. Xue, J. Yan, R. Li, T. Li, and X. Gao, "An ultrathin, dual-band, and dual-polarized metalens antenna based on double-resonant Huygens' metasurface," *IEEE Antennas and Wireless Propagation Letters*, Vol. 23, No. 5, 1473–1477, 2024.

[10] Tutar, F. and G. Ozturk, "An effective metasurface-based linear and circular polarization converter for C- and X-band applications," *Optical Materials*, Vol. 128, 112355, 2022.

[11] Zhou, X., J. Wu, H. Yang, S. Li, Y. Yang, and J. Chen, "A dual-broadband dual-function polarization converter based on reflective metasurface," *Journal of Applied Physics*, Vol. 132, No. 13, 133103, 2022.

[12] Khan, H. A., A. Majeed, H. Zahra, F. G. Kakepoto, S. M. Abbas, and M. Alathbah, "Transparent conformal metasurface absorber for ultrawideband radar cross section reduction," *Journal of Physics D: Applied Physics*, Vol. 57, No. 13, 135105, 2024.

[13] Zhou, Q., W. Ma, T. Wu, Y. Li, Q. Qiu, J. Duan, J. Li, L. Jiang, W. Zhou, Y. Gao, *et al.*, "Metasurface terahertz perfect absorber with strong multi-frequency selectivity," *ACS Omega*, Vol. 7, No. 41, 36 712–36 727, 2022.

[14] Ghosh, S., J. Ghosh, M. S. Singh, and A. Sarkhel, "A low-profile multifunctional metasurface reflector for multiband polarization transformation," *IEEE Transactions on Circuits and Systems II: Express Briefs*, Vol. 70, No. 1, 76–80, 2023.

[15] Agrahari, R., P. K. Rajbhar, M. Mahto, and P. K. Jain, "Metasurface assisted wideband multifunctional polarizer," *Journal of Applied Physics*, Vol. 133, No. 9, 094902, 2023.

[16] Guo, Q., F. Hao, M. Qu, J. Su, and Z. Li, "Multiband multifunctional polarization converter based on reconfigurable metasurface," *IEEE Antennas and Wireless Propagation Letters*, Vol. 23, No. 4, 1241–1245, 2024.

[17] Jin, S., H. Ji, P. Long, B. Liu, R. Luo, T. Xiao, and Z. Zeng, "Reverse design of optical metamaterials for visible-infrared-laser multispectral camouflage with integrated heat dissipation," *Engineered Science*, Vol. 40, 2151, 2026.

[18] Wang, L., C. Xu, J. Liu, Z. Chu, H. Yang, J. Jiang, J. Wang, Y. Jia, S. Sui, Q. Fan, *et al.*, "Flexible multiband stealth metasurface compatible with visible-laser-infrared-microwave spectra," *Photonics Research*, Vol. 14, No. 3, 909–918, 2026.

[19] Liu, D., Y. Wang, K. Ji, H. Gao, S. Zhou, T. Liu, and H.-X. Xu, "Infrared-microwave compatible stealth transparent metasurface with digital camouflage and hybrid absorption-scattering," *Nanophotonics*, Vol. 15, No. 12, e70156, 2026.

[20] Huang, S., X. Jing, J. Liao, H. Lin, W. Zhang, L. Yuan, X. Ma, C. Huang, and X. Luo, "A multispectral-decoupled metastructure for simultaneous camouflage across visible, infrared, laser, and microwave bands," *Advanced Functional Materials*, Vol. 36, No. 47, e75462, 2026.

[21] Liu, H., C. Xiong, X. Du, J. Yin, X. Zhu, P. Qiu, Y. Chen, Y. Shi, and B. Xu, "Machine learning-assisted design of infrared-radar-visible light compatible stealth flexible metamaterial structures," *ACS Applied Materials & Interfaces*, Vol. 18, No. 24, 34 033–34 044, 2026.

[22] Gao, C., T. Lai, L. Peng, X. Zhang, Z. Huang, Z. Wang, X. Pang, S. Zhao, and D. Ye, "Multifunctional intelligent reconfigurable metasurface," *ACS Applied Materials & Interfaces*, Vol. 16, No. 41, 55 675–55 683, 2024.

[23] Xu, H., D. Guan, M. Huang, Y. Xu, Q. Zhang, B. Zheng, P. You, and Y. Liu, "Broadband multifunctional scattering control based on reconfigurable polarization conversion metasurface," *Optics Express*, Vol. 33, No. 23, 49 780–49 793, 2025.

[24] Jiang, R. Z., Q. Ma, Z. Gu, J. C. Liang, Q. Xiao, Q. Cheng, and T. J. Cui, "Simultaneously intelligent sensing and beamforming based on an adaptive information metasurface," *Advanced Science*, Vol. 11, No. 7, 2306181, 2024.

[25] Fang, S., L. Deng, P. Zhang, L. Qiu, H. Xie, S. Huang, J. Du, and Z. Wang, "Dual-function flexible metasurface for absorption and polarization conversion and its application for radar cross section reduction," *Journal of Applied Physics*, Vol. 131, No. 13, 135106, 2022.

[26] Gao, X., X. Han, W.-P. Cao, H. O. Li, H. F. Ma, and T. J. Cui, "Ultrawideband and high-efficiency linear polarization converter based on double V-shaped metasurface," *IEEE Transactions on Antennas and Propagation*, Vol. 63, No. 8, 3522–3530, 2015.

[27] Lin, B., L. Lv, J. Guo, Z. Liu, X. Ji, and J. Wu, "An ultra-wideband reflective linear-to-circular polarization converter based on anisotropic metasurface," *IEEE Access*, Vol. 8, 82 732–82 740, 2020.